CHALMERS
UNIVERSITY OF TECHNOLOGY

Impact of hard-turning parameters on the surface integrity of hybrid 60 steel

Master's thesis in Materials engineering

SOUKAINA BAAZIZ

DEPARTMENT OF INDUSTRIAL AND MATERIALS SCIENCE

CHALMERS UNIVERSITY OF TECHNOLOGY
Gothenburg, Sweden 2024
www.chalmers.se

Impact of hard turning parameters on the surface integrity of hybrid 60

SOUKAINA BAAZIZ

Department of Industrial and Materials Science
CHALMERS UNIVERSITY OF TECHNOLOGY
Sweden 2024

Impact of hard turning parameters on the surface integrity of hybrid 60

SOUKAINA BAAZIZ
Department of Industrial and Materials Science
Chalmers University of Technology

Abstract

This master thesis investigates the surface integrity of hard-turned Hybrid 60, focusing on the effects of machining parameters on the material's microstructure and mechanical properties. Seven samples were machined: samples A, B, C, and D with varying cutting speeds and feed rates, and samples E1, E2, and E3 under identical conditions. To analyze the surface integrity, techniques such as X-ray diffraction (XRD), optical microscopy (OM), scanning electron microscopy (SEM), and energy-dispersive X-ray spectroscopy (EDS) were employed alongside surface roughness measurements. The XRD and topography analyses revealed a characteristic hook-shaped residual stress profile across all samples, with the highest compressive stresses occurring at the subsurface. Notably, samples machined at high feed rates and low cutting speeds exhibited the highest subsurface compressive stresses, while high cutting speeds induced more thermal stresses, resulting in lower surface roughness.

SEM analyses identified a thin, notable layer on the machined surfaces of samples B, C, D, and E1, significantly thinner than the typical white layers observed in hard-turned bearing steels. Interestingly, this thin layer was absent in sample A, which instead showed severe plastic deformation. This variation underscores the influence of different cutting parameters on the material's surface integrity. These findings offer valuable insights into optimizing hard turning processes for Hybrid 60, demonstrating the critical role of machining parameters in influencing the material's microstructural and mechanical behavior.

Key words: Hybrid 60, surface integrity, hard turning.

Table of Contents

Chapter 1

I-Introduction

In the field of material science, the quest for the ideal material for specific applications is ongoing. With each new material discovery, unique challenges arise, particularly regarding how to process and maintain its inherent properties.

One of the primary obstacles is machining, which is affected by a multitude of factors including the material's hardness, thermal properties, chemical composition, and strength. These factors can significantly impact the final product's properties and its surface integrity, necessitating careful consideration and adaptation of machining techniques to preserve the material's original characteristics.

In 2017, Ovako unveiled an innovative material known as Hybrid steel, among which Hybrid 60 stands out for its notable hardness level, indicated by the "60" in its name and it embodies the optimal fusion of characteristics from tool steel, lower alloy engineering steel, maraging steel, and stainless steel, crafted through the innovative blending of carbide hardening and intermetallic precipitation techniques. It is engineered to excel in high-stress environments and boasts an exceptional capacity to endure temperatures up to 500°C [5].

Ovako reports that Hybrid Steel, including the notable Hybrid 60 variant, is amenable to a wide range of machining technologies. Among these, hard machining [1] specifically, hard turning stands out for its applicability to workpieces with a hardness exceeding 45 HRC [2]. This technique is particularly relevant for Hybrid 60, a material about which detailed machining information remains scarce.

Investigating the effects of hard turning on the surface integrity of Hybrid 60, especially when employing various cutting parameters, promises to yield valuable insights. A key tool in this exploration is the IT105 cubic boron nitride (IT105 CBN), recognized for its effectiveness in machining hard materials.

Understanding the interaction between IT105 CBN and Hybrid 60 under different machining conditions will enhance our comprehension of this material's behavior and potential

applications, paving the way for optimized machining strategies that leverage its unique properties.

I.1 Research objectives

The goal of this thesis is to delve into the examination of surface integrity for Hybrid 60, a material characterized by its martensitic structure, which is the result of its unique dual hardening mechanisms This study focuses on the effects of various hard turning parameters, including tool wear, on the machined surfaces. Given the transformative impact of machining on the material's microstructure, understanding these changes is crucial for predicting the resultant surface characteristics and overall integrity.

This research aims to dissect the specific alterations and resultant traits of the Hybrid 60 surface post-machining. By delving into the microstructural evolution induced by machining, this study seeks to illuminate the knotted interplay between machining parameters and surface integrity. Consequently, this thesis proposes to answer the following research question:

- "How do varying hard turning parameters and tool wear specifically influence the microstructure, and consequently, the surface integrity and characteristics of Hybrid 60?"

Chapter 2

II- Literature review

II-1 Heat treatment

II-1-1 Precipitation hardening

Precipitation hardening encompasses both the precipitation of carbides, which is also known as secondary hardening, and the formation of intermetallic compounds that enhance the material's strength. [3,4]

Secondary hardening in steel is advantageous for applications at elevated temperatures. This process begins with austenitization, followed by quenching and tempering. During this phase, alloy carbides, formed from elements such as molybdenum, chromium, and vanadium in controlled quantities, precipitate at designated temperatures [3.4.5]. This precipitation significantly enhances the steel's hardness and strength, rendering it more durable and resistant to wear in challenging conditions [3,4].

Intermetallic strengthening enhances superalloys, like maraging steel and Ni-based alloys with a low carbon content, through the formation and distribution of intermetallic compounds within their matrix during tempering. These compounds, stable and coherent with the matrix, significantly improve the alloys strength and thermal stability [6,7].

II-1-2 Heat treatment of Hybrid 60

Hybrid steel employs a heat treatment process akin to that of dual-phase steel, emphasizing the role of intermetallic precipitation and secondary hardening as key mechanisms for enhancing strength [3,9]. According to Avako, the production of Hybrid steel can be streamlined into a three-step process, beginning with forging, followed by machining, and concluding with aging. This approach is more efficient than conventional methods, which typically require additional steps [8].

The heat treatment process for Hybrid 60 involves austenitization at a temperature of 1020°C for 45 minutes. This step is crucial for achieving a martensitic matrix characterized by minimal distortion and superior dimensional stability; thanks to the strategic use of alloying elements. The process continues with air cooling to facilitate this transformation [5]. Subsequently, the steel undergoes tempering, a procedure conducted at temperatures ranging from 520°C to 570°C for four hours, followed again by air cooling. This phase of the heat treatment ensures the attainment of a final hardness level of 690 HV (Vickers Hardness), optimizing the material's mechanical properties for durability and performance [5].

II-2 residual stresses and surface roughness

The surface integrity of a material is critically important due to its significant impact on fatigue performance. Experimental evidence has shown that factors such as residual stresses and surface roughness are essential in determining the fatigue behavior of materials [17].

II-2-1 Residual stresses

Residual stresses, which may be either compressive or tensile, originate from inhomogeneous plastic deformation caused by mechanical and thermal loads during the machining process. Compressive residual stresses are typically advantageous, enhancing the fatigue life of a component and its resistance to stress-corrosion cracking. Conversely, tensile residual stresses are often harmful and negatively affecting these properties [18].
In the study of Hybrid 60 steel, understanding residual stresses plays an important role. According to Loaiza Uribe [19], Hybrid 60 outperforms conventional materials like AISI 52100 steel and Hardox 400, showing remarkable resistance to microstructural decay under rolling contact fatigue (RCF) conditions. This durability is linked to its distinctive microstructure and the presence of stable alloy precipitates such as NiAl and M_7C_3, which resist dissolution during cyclic loading, thus improving its fatigue performance. When subjected to RCF testing across a range of contact pressures, Hybrid 60 displayed a significantly lower area fraction of material decay compared to AISI 52100 steel and Hardox 400 [19]. This indicates Hybrid 60's superior ability to resist the negative impacts of residual stresses and maintain its structural integrity under conditions of high stress. The presence of specific alloy precipitates in Hybrid 60 endows it with increased resistance to decay induced

by cyclic loading, distinguishing it from other materials prone to significant microstructural degradation and diminished fatigue life [19].
The influence of machining parameters on the induction of surface residual stresses is significant. In an experiment conducted by Sutanto and Madl [18] on the AISI 52100 steel surface, it was found that increasing in both the feed rates and the cutting speed leads to a reduction in residual stresses [18]. This phenomenon is primarily due to the heat generated during the machining process [18]. As the cutting speed escalates, so does the temperature, which subsequently affects the nature of the residual stresses whether they become tensile or compressive. The determining factor for this effect is the extent of the permanent plastic deformation zone created during machining, which is influenced by the mechanical and thermal loads applied. When these loads remain below the yield strength of the material, the result is the formation of compressive residual stresses on the surface of the workpiece [18].

II-2- 2 Surface roughness

Surface roughness plays a critical role in the industrial sector due to its significant impact on functional properties such as surface fatigue life, corrosion resistance, and friction [21]. This concept involves consistent or sporadic deviations from an ideal surface, contributing to the surface's three-dimensional topography [20].

The influence of machining methods and parameters beside the tools utilized is profound on surface roughness, highlighting the importance of optimizing these factors for improved outcomes. Specifically, the primary machining parameters investigated in the context of hard turning of hardened steel include the feed rate, cutting speed, and depth of cutting. These parameters are crucial in determining the final surface integrity [13].
In research conducted on AISI 52100 steel, Jouini et al. [22] demonstrated that the fatigue life of bearing components made from this steel improved as the surface roughness, measured as Ra, decreased. This finding underscores the direct relationship between surface roughness and component longevity. Additionally, a separate study focusing on EN31 alloy steel, a high-strength steel with a hardness exceeding 60 HR, revealed that surface roughness increased with the feed rate across various cutting speeds and depths of cut [13].

II-2-3 White Layers

White layers, also known as white etching layers (WEL), are thin, hard, and featureless alterations observed in various ferrous materials subjected to processes such as hard turning, grinding, drilling, electrical discharge machining, equal channel angular pressing, and ball-end milling. When examined in cross-section under an optical microscope in polished and etched conditions, these layers appear white, hence their designation.

The microstructure of a white layer differs significantly from that of the underlying base material, potentially affecting the surface properties of the machined part. Typically, the thickness of these layers' ranges from 5 to 25 micrometers [24].

Regarding grain size, white layers often consist of ultra-fine grains ranging from several hundred nanometers to a few micrometers [24].
The formation of white layers is primarily driven by two mechanisms, influenced by various factors including the cutting tool's edge, heating rate, cooling rate, pressure, and the duration of contact between the cutting tool and the workpiece surface:

1. Thermally Induced White Layer: This type results from phase transformations due to rapid heating and quenching due to the increased thermal load during machining which significantly impacts the residual stresses (notably tensile residual stresses are observed) and the retained austenite content on the material's machined surface [24].
2. Mechanically Induced White Layer: This type of layer is formed through severe plastic deformation of the surface resulting from the mechanical stress and strain during machining. This intense activity cause dynamic recrystallization, which leads to a fine-grained microstructure [24].

Chapter 3

III-Material and Methodology

III-1 Hard turning

Hard turning is a precision machining process specifically designed for the removal of excess material from workpieces [10]. It is characterized by its single-point cutting technique, where tools with precisely defined, geometric cutting edges are employed to shape metallic materials. Typically, this process is applied to materials with a hardness of around 45 HRC [11,12], making it suitable for a wide range of industrial applications. The use of cutting tools with well-defined edges allows for high precision and minimal material waste [10], enhancing the efficiency and quality of the machining process. Furthermore, hard turning is often favored for its ability to produce fine finishes and maintain tight tolerances, reducing the need for subsequent grinding or finishing processes.

The precision of the final machined workpiece is predominantly affected by three critical dependent input parameters: feed rate (f), cutting speed (v_c), and depth of cut (ap). Each of these factors plays a vital role in determining the tolerances and overall quality of the machining process [13], and the combination of different values of these factors help with finding an optimized surface for different applications. However, to obtain the desired surface integrity, other parameters need to be well considered which are: cutting tool materials, geometry and conditions. Additionally, achieving optimal surface integrity requires careful consideration of other critical aspects, including the material, geometry, and condition of the cutting tool.

In this thesis, various combinations of these elements are chosen for each ring under investigation. This approach is adopted to gain a deeper insight into how these elements affect the surface integrity of Hybrid 60. The testing matrix is illustrated in Figure 1 and the details of the experimental parameters are provided in Table 1.

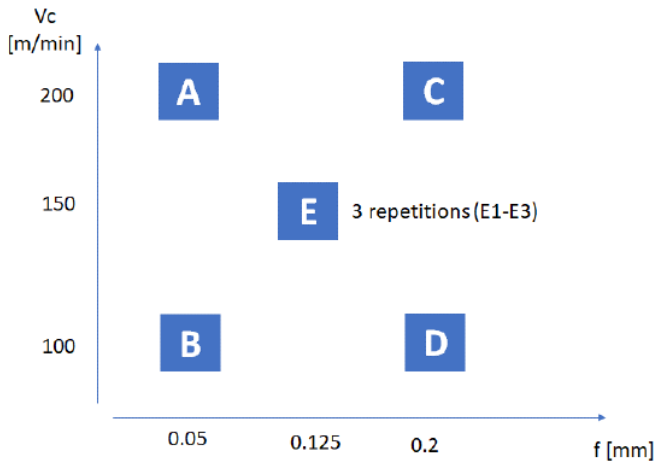

Figure 1: Hybrid 60 testing matrix

Table 1: Test parameters to study the role of cutting speed and feed rate on the surface integrity of H60

Test matrix Sample	**Cutting speed (m/min)**	**Feed rate (mm/rev)**	**Tool wear (mm)**	**NL angle**	**Pressure (bar)**	**Depth of cut (mm)**
A	200	0,05	0	15	20	0,1
B	100	0,05	0	15	20	0,1
C	200	0,2	0	15	20	0,1
D	100	0,2	0	15	20	0,1
E1	150	0,125	0	15	20	0,1
E2	150	0,125	0	15	20	0,1
E3	150	0,125	0	15	20	0,1

III-1-1 Tool Material

The inserts used in this experiment are the innovative CBN (Cubic Boron Nitride) grade IT105, which is designed specifically for the finish turning of heat-resistant alloys, boasting a cutting speed of up to 300m/min. This grade not only achieves unmatched productivity and stability but also ensures a longer tool life and superior surface finish quality compared to ceramic and other PCBN grades [15].

III-1-2 Tool wear

Tool wear poses a significant challenge in the machining of hardened steels, presenting obstacles that impact both the efficiency and quality of the machining process and the surface integrity of the machined material. This phenomenon is categorized into three primary groups: thermal wear, adhesion, and mechanical wear. Each of these categories encompasses subgroups, highlighting the multifaceted nature of tool wear mechanisms [16]. Importantly, the extent and rate of wear across these groups and their subgroups are directly influenced by the cutting parameters, which include cutting speed, feed rate, and depth of cutting. This categorization not only aids in understanding the underlying causes of tool wear but also facilitates the development of strategies to mitigate wear and extend tool life in the machining of hardened steels.

In the case of Hardened steel flank wear (occurs parallel to the cutting edge) and crater wear (wear on the rake face), are of particular interest because they occur universally across all conventional cutting operations. Other types of wear are typically more specific, affecting only certain tool-work material combinations or specific machining processes [25].

III-2 Workpiece material

The innovative Hybrid Steel 60 has garnered considerable attention due to its exceptional characteristics, making it an interesting subject for research to understand its behavior and interactions during machining and application processes. The unique chemical composition of Hybrid 60 (Table 2), which includes a distinctive mix of alloying elements, gives it its specific strength and hardness, making it a material of interest for further study and use in various applications.

Table 2 – Composition of hybrid 60

Element	**C**	**Si**	**Mn**	**Cr**	**Ni**	**Mo**	**V**	**Al**
Wt.%	0.28	0.1	0.3	5	6	0.7	0.5	2

III-2-1 Hybrid 60 microstructure

Hybrid 60 features a lath martensitic matrix as can be seen in Figure 2, which emerges due to the material's low carbon content (0.28% C) and its high martensite transformation temperature (350°C) [5]. This matrix is interspersed with precipitates, including M_7C_3 carbide, as well as intermetallic precipitates like NiAl [5]. Additionally, a minor quantity of undissolved precipitates, predominantly MC, originally formed during the soft annealing process, persists even after undergoing solution treatment [23].

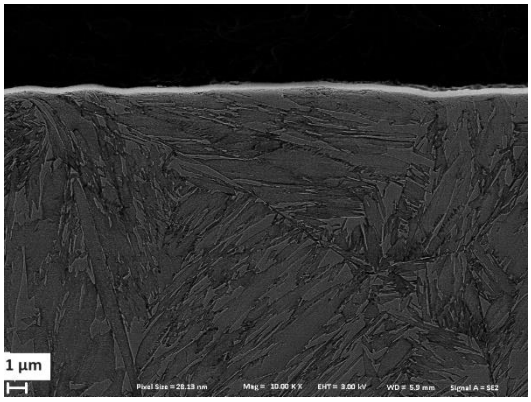

*Figure 2: SEM image of sample **B***

III-2-2 Hybrid 60 properties

Hybrid 60 has outstanding properties, particularly excelling over AISI 52100 steel in high-temperature applications due to its superior yield strength and stable microstructure post-tempering [5]. This enhanced stability ensures optimal performance compared to AISI 52100 steel.

Chapter 4

IV- Experimental details

To thoroughly characterize the surface integrity of hard turned Hybrid 60, a comprehensive series of tests and measurements were conducted. The process began with residual stress assessments, followed by detailed surface topography analysis. Subsequent steps involved cutting the material and preparing samples for further examination. Advanced imaging techniques, including Optical Microscopy (OM) and Scanning Electron Microscopy (SEM), were employed to inspect the microstructural details. Hardness measurements and stereo microscopy were also carried out. These investigative techniques were integral in gaining insights into the material's behavior post-machining and understanding the impact of various machining parameters on the surface under study.

IV-1- Residual stresses measurements using X-ray Diffraction

IV-1-1- General information

X-ray diffraction (XRD) is a sophisticated method utilized within various industries to assess residual stresses that occur due to manufacturing processes like heat treatment and machining. This technique fundamentally involves the measurement of strain within the crystal structure of materials, from which residual stresses are inferred. These stresses, although not directly measurable as they are an extrinsic property, are calculated based on observed strain, which represents a change in the crystal lattice typically viewed as linear and elastic deformation.

Figure 3: XRD system used to measure the residual stresses

The application of XRD for stress analysis is detailed in academic works, such as the one by Noyan and Cohen. In practice, X-rays target the material undergoing testing, interacting with its atomic structure. This interaction prompts an electron to leave its outer shell, leading to the emission of a scattered X-ray beam. Only the scattered rays that satisfy Bragg's Law are recorded, creating a diffraction peak that corresponds to specific lattice planes.

In XRD setup use which is a MiniFlex from Rigaku, the scale of the X-ray beam can vary. Portable lab-XRD systems, for instance, use a cone-shaped collimator that adjusts to project a circular spot ranging from 0.5 to 5 mm in diameter on the material’s surface. In contrast, stationary systems may produce a rectangular or square beam. The detection of these diffraction peaks is carried out by a CCD device equipped with multiple channels that capture photon activity, indicating the presence of residual stresses based on the peak shifts observed. These shifts denote whether the material's lattice is under compression or tension, providing valuable insights into the internal stress states of the material.

Three randomly chosen points, on the machined surfaces of the seven samples (A; B; C; D; E1; E2; E3), were selected for X-ray Diffraction (XRD) measurements to obtain an average value of the residual stresses. Prior to these measurements, the specimens were cleaned with isopropanol to eliminate any surface dust that could potentially compromise the results. Subsequent depth profiling involved the use of two electropolishing methods starting with a saturated salt electrolyte followed by perchloric acid electrolyte. Depth measurements were

precisely taken at six points—0, 5, 10, 20, 50, and 100 µm—using a dial gauge. For the XRD analysis, a chromium K-alpha (Cr-Kα) source equipped with a 2mm collimator was employed, utilizing a tilt angle range from -45° to 45°.

IV-2- Surface roughness

The surface topography of the workpieces was analyzed using a Sensofar microscope, equipped with a Nikon 10x magnification lens. The analysis employed Vertical Scanning Interferometry (VSI), also known as White Light Scanning Interferometry, utilizing Mountains Map 8.2 software for data processing. To achieve a comprehensive and representative analysis, each specimen was measured three times, allowing for an average assessment of surface characteristics. For each measurement, both visual images and statistical data were systematically recorded.

IV-3- Sample preparation

The samples were initially sectioned using a precision cutting machine at a low feed rate to minimize heat generation during cutting, thereby preserving the microstructure of the material. The cross-sections of the samples were encapsulated in a mounting press, where PolyFast epoxy resin was used. This assembly was subjected to a temperature of 180°C under a pressure of 200 bar for two minutes, facilitating the resin to melt, followed by a cooling period of three minutes to solidify the mount.

Subsequently, the sample underwent a four-stage polishing process amounting 20 minutes. The initial coarse polishing was performed for 5 minutes using 220 grit designed for heavy material removal, employing water as a lubricant. This was followed by a medium polishing for 5 minutes on a resin-bonded diamond disc using a 9 µm water-based diamond suspension. The third polishing used 3µm diamond suspension. The final fine polish, intended to achieve a mirror-like finish free of scratches, was conducted for 5 minutes using a 1 µm diamond suspension. After polishing, the sample was cleaned with ethanol and air-dried to prevent any residue from affecting subsequent analyses. The result was a highly polished surface with a reflective finish.

IV-4- Optical Microscopy and Scanning Electron Microscopy (SEM) analysis

To expose the microstructural features for optical microscopy, the samples were etched with 2% Nital solution. They were immersed in this etching solution for 20 seconds, followed by thorough rinsing with ethanol and water to remove any residual chemicals.
Optical microscopy (OM) relies on visible light and a series of lenses to view samples. Typically, illumination comes from sources like bulbs or LEDs. High-end microscopes usually incorporate three main lenses: an objective lens to gather light, an eyepiece lens to deliver a clear image, and a condenser lens to focus light onto the sample.
Optical microscopy was employed to analyze the cross-sectional microstructure and inspect the microstructural characteristics of the machined surfaces.
For the SEM analysis, the LEO 1550 SEM was utilized to characterize the machined surfaces. Equipped with an EDS detector, this instrument allows the chemical analysis of the surface. Chemical profiling of the cross-section was conducted using point and line analysis as well as spectral mapping.
Scanning electron microscopy (SEM) offers a more advanced imaging technique than optical microscopy (OM) by using electrons instead of light. In SEM, electrons are emitted from a source, accelerated, and focused onto the specimen. The interaction of these electrons with the specimen generates different signals, such as backscattered electrons and secondary electrons, each revealing various details about the sample.
Backscattered electrons, with their higher energy, originate from deeper in the material and image, differences in atomic number. Secondary electrons, on the other hand, offer detailed topographic information. The type of detector used in SEM determines the kind of contrast and information obtained in the images. In this thesis only secondary electrons imaging was used.

IV-5- Hardness measurements

The hardness of Hybrid 60 samples was measured using the Vickers hardness test. Vickers hardness measures the resistance of a material to deformation using a diamond pyramid indenter under a specific load. The resulting diagonal length of the indent are used to calculate the hardness value, providing a precise metric for material strength.

Hybrid 60 is known to have a hardness of 60 HRC, which will be compared to the Vickers hardness values obtained.

During the test a load of 1 kilogram-force (HV) was applied during the test, and the measurements were observed at a magnification of 20x to ensure accuracy.

Chapter 5

V- Results

V-1- Residual stresses

the residual stresses measurements conducted on the surface in addition to the residual stress depth profiling are shown in Figure 4 and Figure 5 respectively. (Sample A, characterized by a high cutting speed (v_c) and low feed rate (f); Sample B, with low v_c and low f; Sample C, featuring high v_c and high f; Sample D, with low v_c and high f; and Sample E (1, 2, 3), which has medium v_c and medium f). Additionally, a heat-treated sample was analyzed to provide a baseline for comparison.

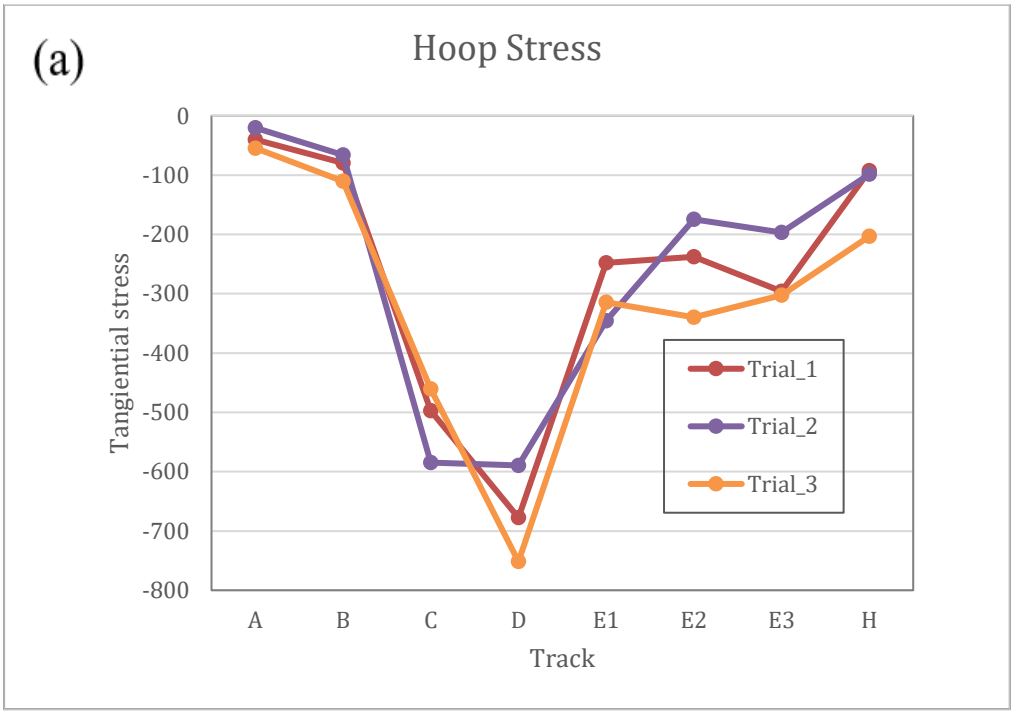

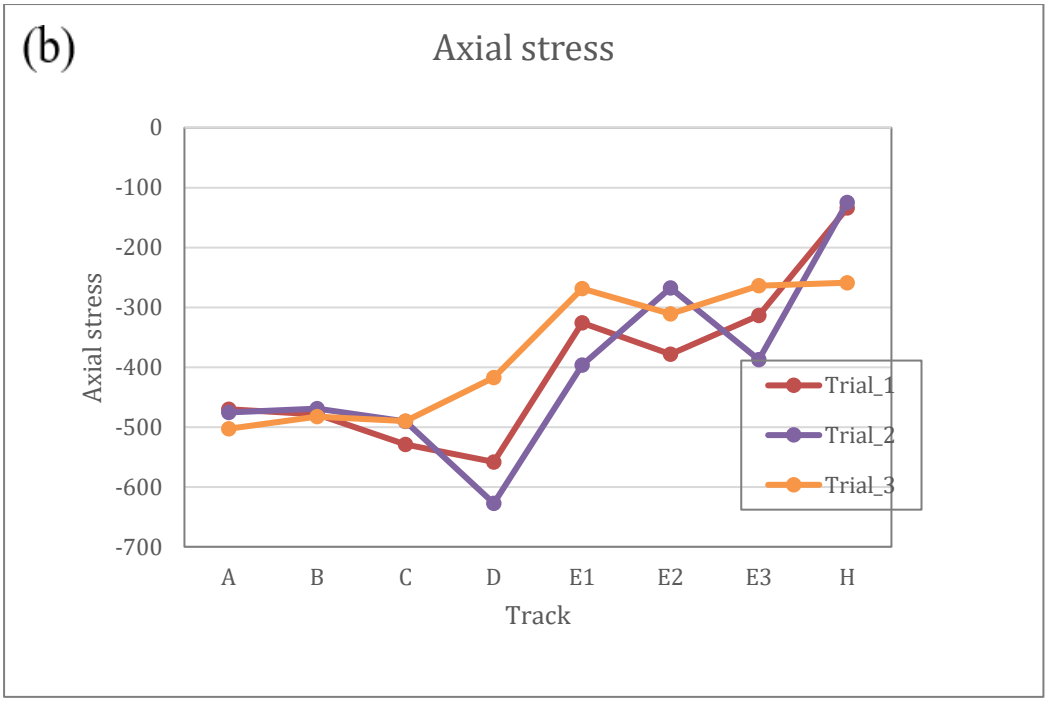

Figure 4: Residual stresses on the machined surface of samples A, B, C, D, E1, E2, E3, and H, (a) Hoop stress (b) Axial stress

The surface residual stresses measured in the cutting direction (hoop stresses) and feed direction (axial stresses) for all samples are predominantly compressive. Sample D, with a low cutting speed and high feed rate, exhibits the highest compressive stresses in both the cutting and feed directions. Sample C also displays high compressive stresses in both directions. In contrast, Samples A and B, which have low feed rates coupled with high and low cutting speeds respectively, show minimal compressive stresses nearing zero in the cutting direction, while maintaining very high compressive stresses in the axial direction. Samples E1, E2, and E3, characterized by medium feed and cutting speeds, exhibit comparably high residual stresses in both directions, approximately 320 MPa in the feed direction and 265 MPa in the cutting direction. The heat-treated sample, sample H, also demonstrates surface compressive stresses, with values of 172 MPa in the feed direction and 131 MPa in the cutting direction.

The residual stress depth profiles in both the cutting and feed directions are illustrated in Figure 5, providing a detailed understanding of the stress distribution induced by different machining parameters. In the feed direction, all samples exhibit significant compressive stresses on the machined surface, with sample D, machined at a high feed rate of 0.2 mm/rev and a low cutting speed of 100 m/min, showing the highest compressive stress value of -549 MPa. As the distance from the surface increases, these compressive stresses tend to shift,

eventually transitioning to tensile stresses at greater depths. The residual stress profiles along the cutting direction exhibit a distinct trend compared to those in the feed direction. All samples show high compressive residual stresses, with sample D, machined at a high feed rate and low cutting speed, displaying the most pronounced stresses. These stresses reach their peak at a depth of 5 µm, in contrast to the feed direction, where the highest compressive stresses are found on the surface rather than in the subsurface.

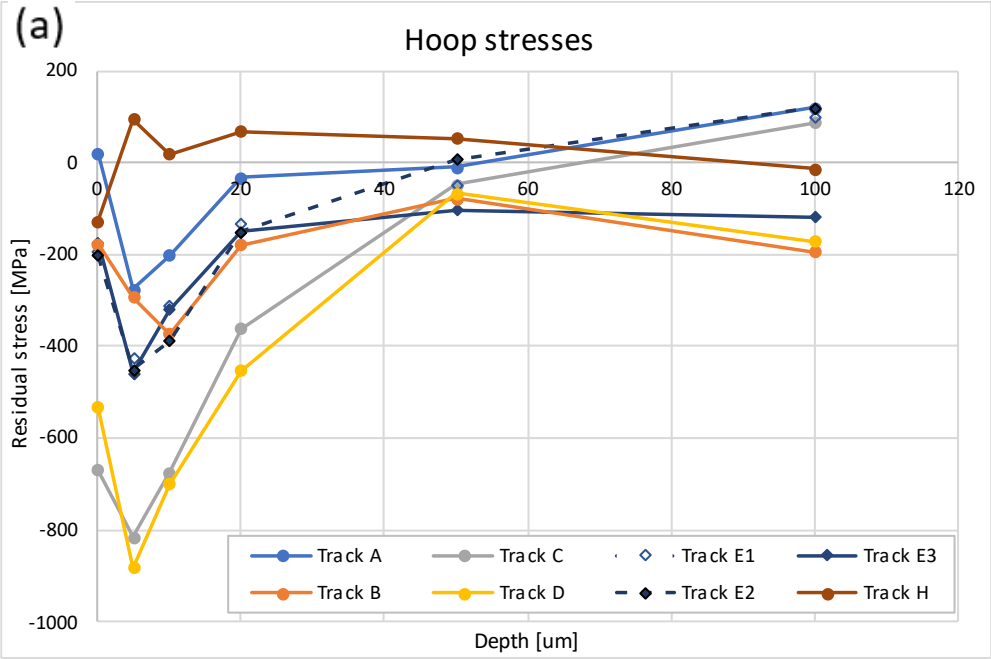

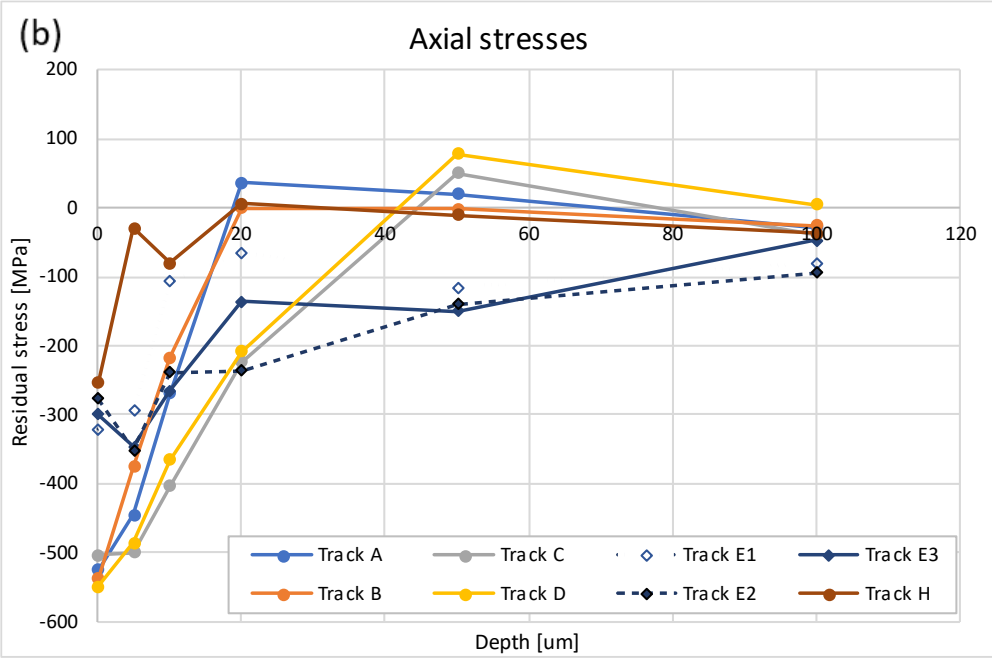

figure 5: Residual stress depth profiles for the different samples (A, B, C, D, E1, E2, E3). (a) Hoop stress, (b) Axial stress.

V-2- Surface roughness

The surface roughness, Ra (Roughness average), represents the arithmetic mean of the absolute values of the surface profile's deviations from the mean line. This parameter is crucial in assessing the quality of the machined surfaces. The results obtained for different samples are illustrated in Figure 6.

The surface roughness values for each sample varied significantly, highlighting the influence of cutting parameters on the surface integrity. Sample A, which had a high feed rate and low cutting speed, exhibited the lowest surface roughness with an Ra value of 0.123 µm. This suggests that the combination of these parameters produced a smoother surface profile. Conversely, Sample C, which was machined with the highest cutting speed of 200 m/min and a low feed rate of 0.05 mm/rev, showed the highest surface roughness with an Ra value of 1.065 µm. This indicates that the high cutting speed, even with a low feed rate, significantly increased the surface roughness, possibly due to higher thermal effects and vibrations during machining.

Sample B, machined with both low cutting speed and feed rate, had a surface roughness value of 0.145 µm. This relatively low roughness indicates that slower machining parameters tend to produce a smoother surface. Sample D, with a low cutting speed and high feed rate, had a

roughness value of 1.026 µm, which is quite high, suggesting that a high feed rate has a more detrimental impact on surface smoothness when combined with a low cutting speed.
Sample E1, machined with medium cutting speed and feed rate, had a surface roughness of 0.471 µm. This intermediate value demonstrates that moderate machining conditions result in moderate surface roughness, balancing between the extremes observed in other samples.
The results indicate that lower feed rates and cutting speeds generally result in lower surface roughness, while higher feed rates and cutting speeds increase surface roughness. Sample C exhibited the highest surface roughness due to its high cutting speed, while Sample A had the smoothest surface due to its combination of high feed rate and low cutting speed. These findings emphasize the importance of optimizing machining parameters to achieve the desired surface quality in hard-turned Hybrid 60 steel.

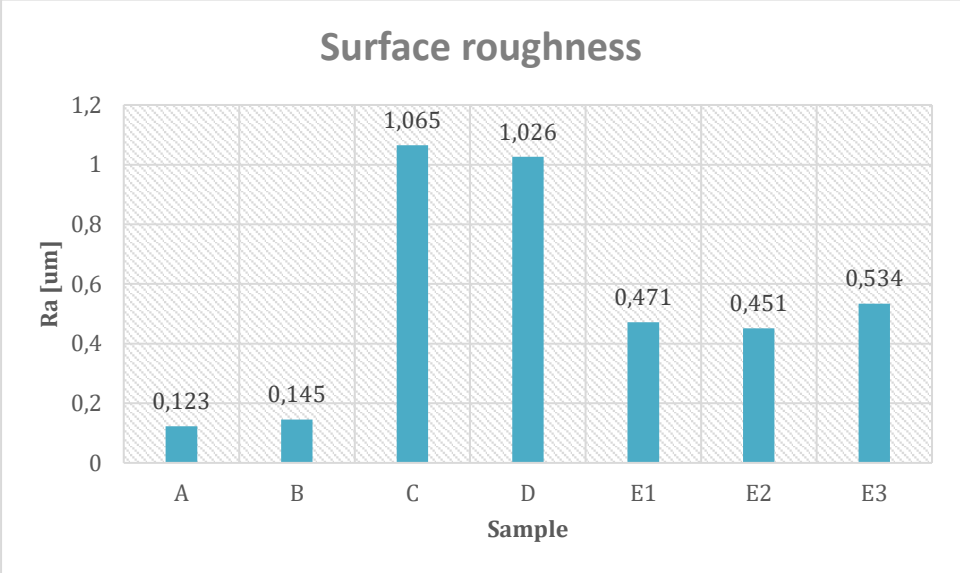

Figure 6: Surface roughness values for samples machined with different cutting speeds and feed rates

Table 3 contains additional surface roughness parameters results from the measurements conducted.

Table 3: Surface roughness parameters for samples A, B, C, D, E1, E2, E3 respectively

Sample	Ra[mean]	Ra[Std dev]	Rv[mean]	Rv[Std dev]	Rz[mean]	Rz[Std dev]	Sa	S10z	Sq
	µm	µm	µm	µm	µm	µm	µm	µm	µm
A	0,123	0,002	0,362	0,011	0,701	0,015	0,226	1,892	0,281
B	0,145	0,002	0,459	0,009	0,939	0,023	0,249	2,082	0,309
C	1,065	0,009	1,714	0,021	4,256	0,025	1,118	6,168	1,328
D	1,026	0,006	1,64	0,023	4,27	0,055	1,206	7,534	1,48
E1	0,471	0,01	0,92	0,026	2,008	0,035	0,548	3,841	0,667
E2	0,451	0,013	0,927	0,018	2,249	0,024	0,488	3,497	0,594
E3	0,534	0,008	1,017	0,027	2,305	0,043	0,588	4,039	0,709

V-3- Optical microscopy

To analyze the metallurgical behavior of the machined surface, optical microscopy was performed on five selected samples: A, B, C, D, and E1. Sample E1 was chosen randomly from a set of three identical samples (E1, E2, and E3). Additionally, the cross-section of the cutting direction of sample B was examined.

The optical microscopy analysis of the machined surfaces revealed only a few discernible features. The primary observation was the bulk microstructure, which was composed predominantly of martensitic laths. These laths are a characteristic feature of the hardened material, indicating the presence of a martensitic phase that formed due to the heat treatment process. Despite the high magnification, Despite the high magnification, no significant surface anomalies or defects were detected, and importantly, there were no white layers or other notable features typically associated with machining-induced alterations as can be seen in Figure 7.

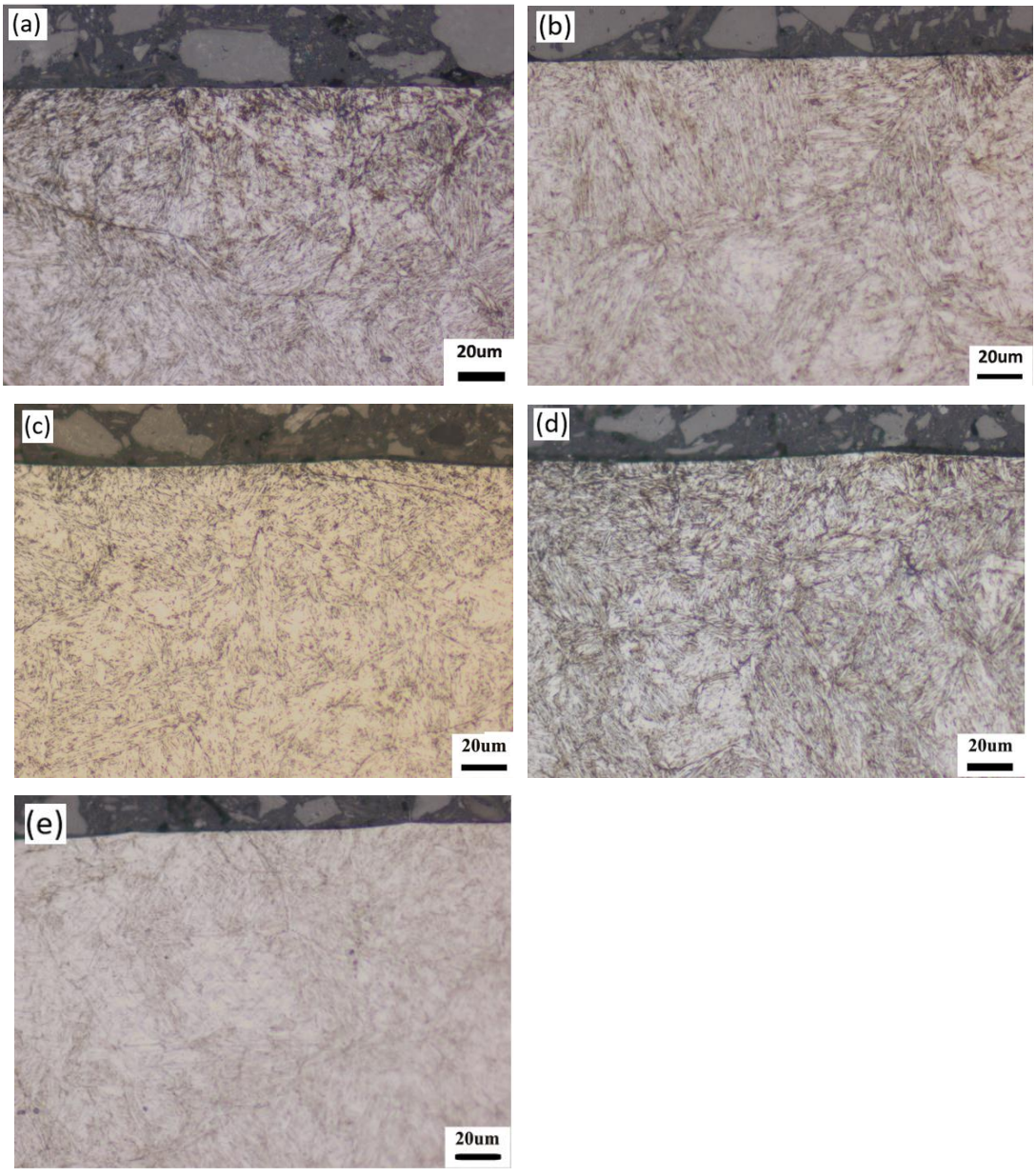

Figure 7: Optical microscopy images, (a) sample A, (b) sample B, (c) sample C, (d) sample D, (e) sample E1.

V-4- SEM & EDS

V-4-1 SEM

As the optical microscopy revealed no features on the machined surfaces, scanning electron microscopy (SEM) was conducted to closely examine the machined surface. Figure 8 shows the SEM images for samples A, B, C, D, and E1.

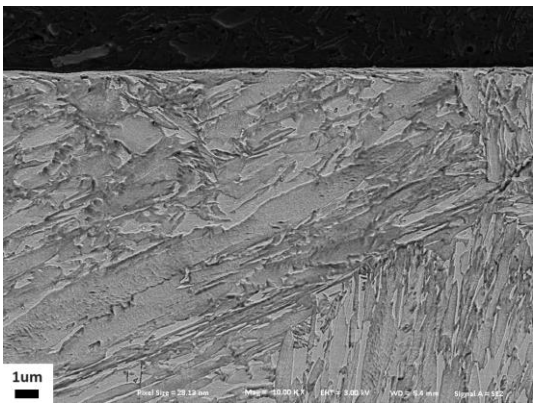

(a)

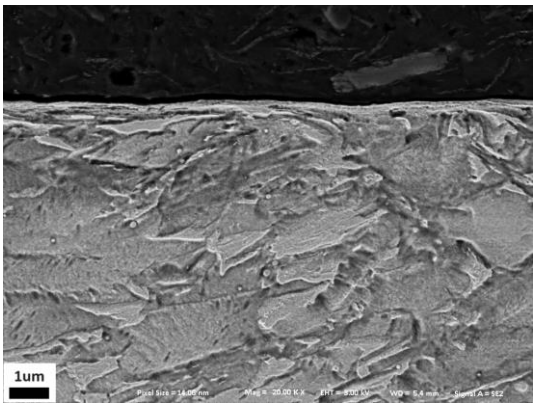

(b)

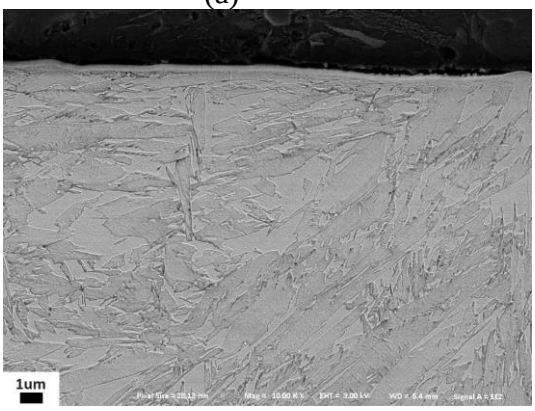

(c)

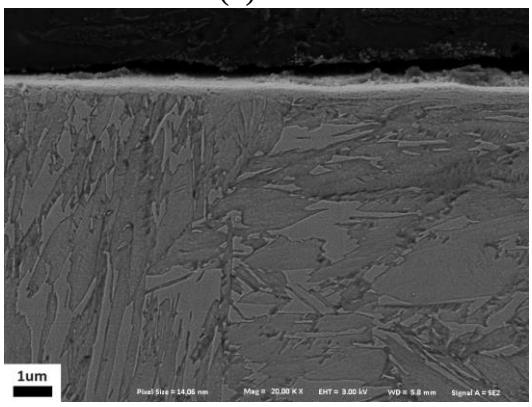

(d)

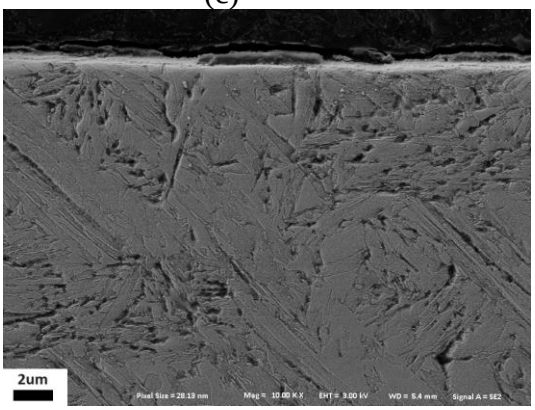

(e)

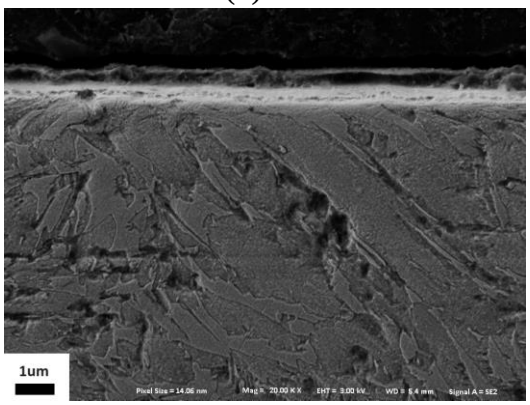

(f)

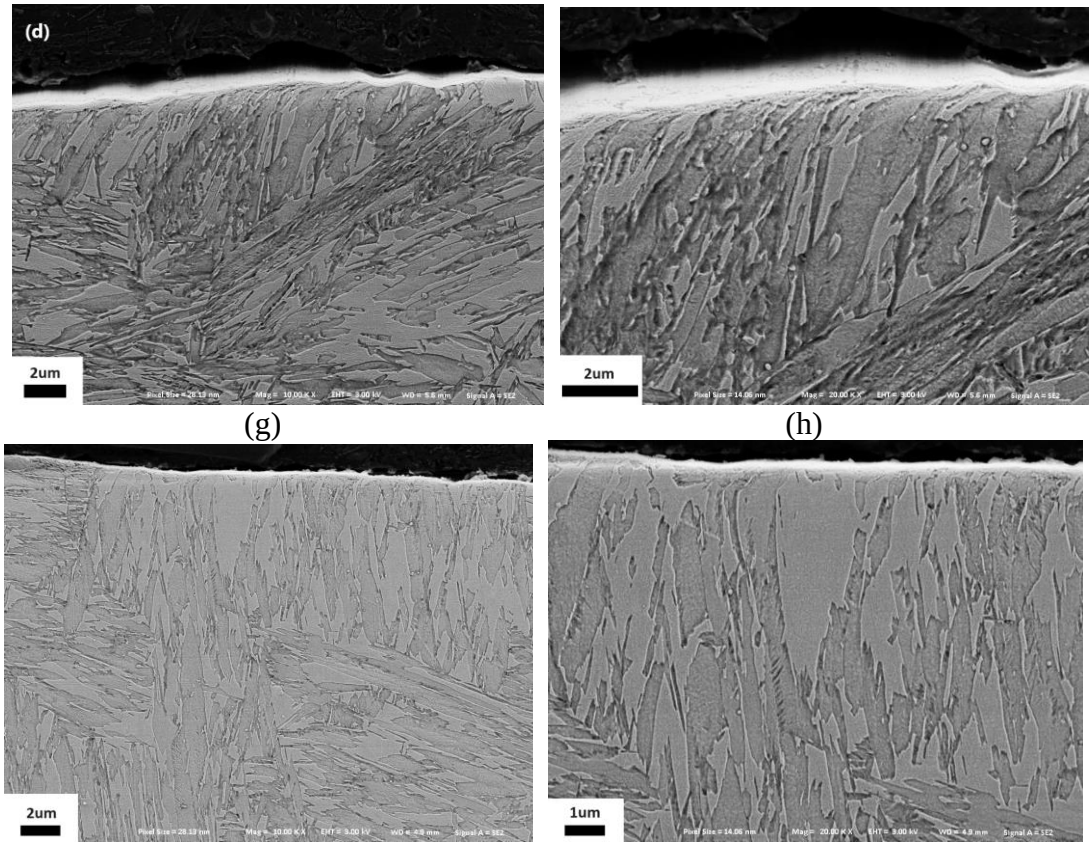

Figure 8: SEM images for each sample at 10k and 20k magnifications (a) sample A at 10k, (b) sample A at 20k, (c) sample B at 10k, (d) sample B at 20k, (e) sample C at 10k, (f) sample C at 20k, (g) sample D at 10k, (h) sample D at 20k, (i) sample E1 at 10k, (j) sample E1 at 20k

For sample A, a noticeable feature is the presence of what appears to be pulling, which can be identified as severe plastic deformation. This deformation is particularly evident in Figure 9. Sample A was machined under high cutting speed (200 m/min) and a low feed rate (0.05 mm/rev), conditions that likely contributed to the observed surface characteristics.

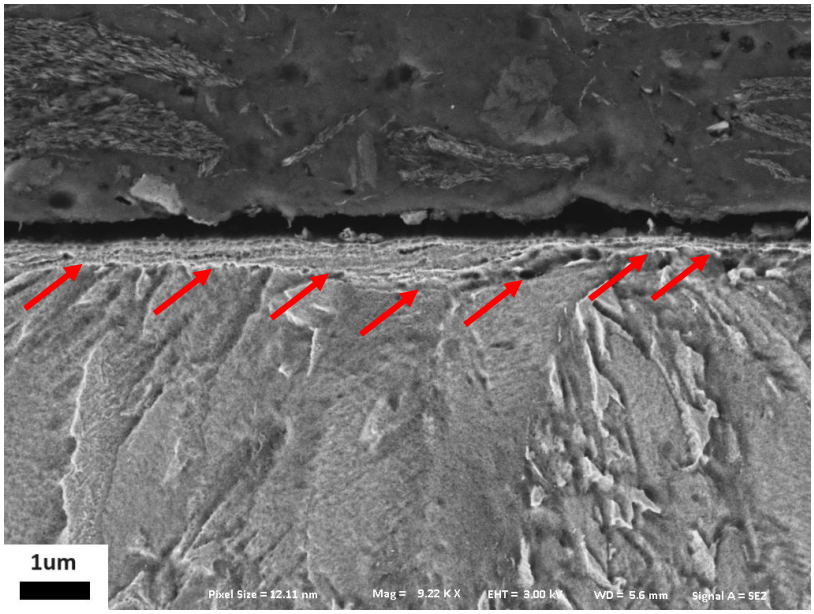

Figure 9: SEM image of sample A

In contrast, the other samples (B, C, D, and E1) displayed a bright layer on the machined surface. Beneath this bright layer, there is a very thin layer that appears to exhibit microstructural refinement. This suggests that the machining parameters for these samples induced changes in the surface microstructure, leading to a refined microstructure layer just below the machined surface. The presence of this refined layer indicates the influence of the different cutting speeds and feed rates used for these samples in altering the surface characteristics.

Upon examining the SEM images of the samples, features resembling cracks were observed in some images, as depicted in Figure 10. These cracks are situated within the bulk material rather than on the machined surface, indicating that their origin is likely unrelated to the surface machining process. Instead, these cracks may have been introduced during the manufacturing of the material itself.

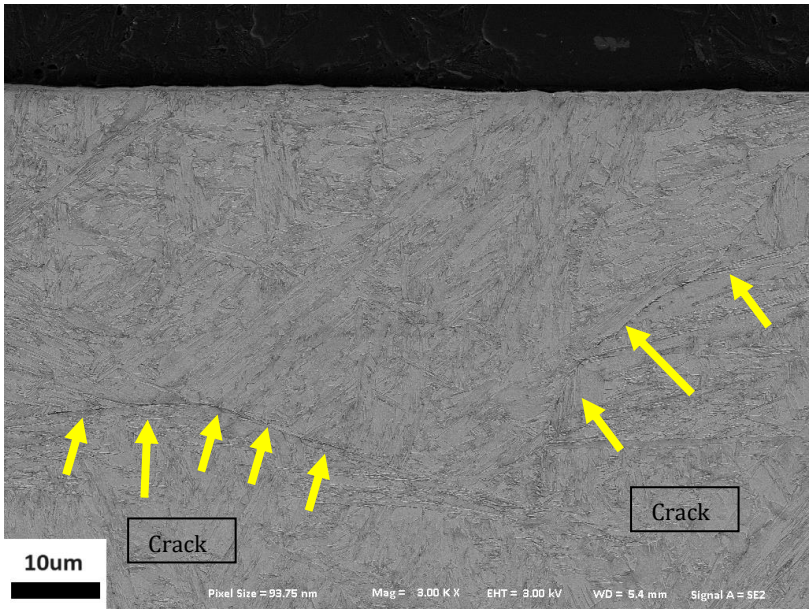

Figure 10: SEM image of sample B showing crack in the bulk material

In addition to the observed cracking in the bulk material, relatively large and randomly distributed shapes were identified, as the SEM image in Figure 11 shows. To determine the nature and composition of these inconsistently appearing structures, EDS analysis was conducted. The detailed results of this analysis are presented in the EDS section.

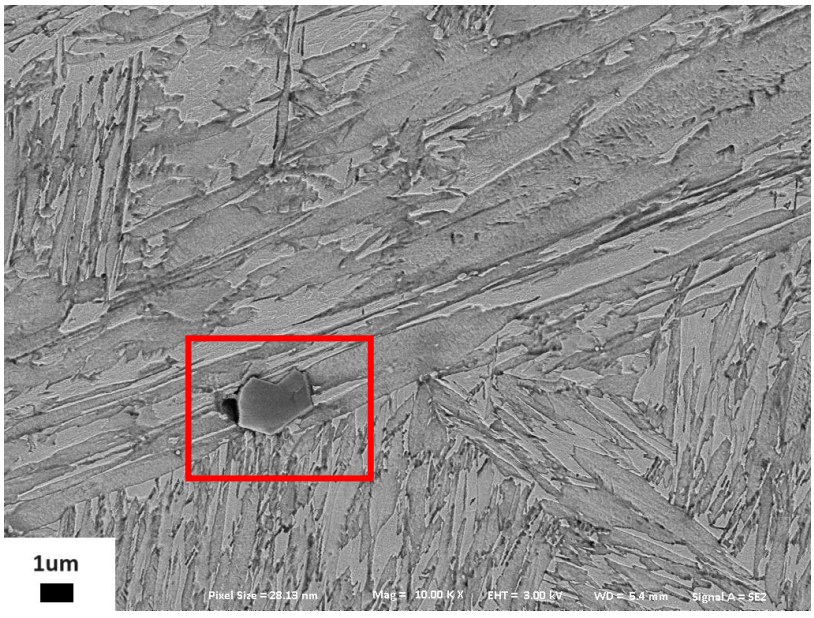

Figure 11: SEM image of a particle in sample A

V-4-2 EDS analysis

To identify and characterize the bright layer observed on the surface, Energy Dispersive X-ray Spectroscopy (EDS) analysis was conducted. This analysis aimed to gather detailed information about the chemical composition of the bright layer. The results obtained from the EDS analysis are presented below.

The EDS analysis was performed on both the surface layer and the bulk material. By examining these different regions, the aim was to gain a comprehensive understanding of the material's behavior and composition. The surface analysis focused on the bright layer, providing insights into its elemental composition, which is critical for understanding the effects of machining parameters on surface integrity. Meanwhile, the bulk analysis offered a comparative perspective, revealing the overall material composition and highlighting any compositional differences between the surface and the bulk.

The collected data from the EDS analysis helps in determining whether the bright layer has a distinct chemical composition compared to the underlying bulk material. This information is important for elucidating the mechanisms behind the formation of the bright layer and its potential impact on the material's performance and durability. By combining surface and bulk analyses, we can better understand how machining processes influence the chemical and microstructural properties of the material, leading to more informed decisions in optimizing machining parameters for Hybrid 60 steel.

Three spectra were obtained from the bulk material (see Figure 12), and the results showed slight variations but were generally consistent with the provided chemical composition of the material, as indicated in Figure 13. For the machined surface, six spectra were analyzed using EDS, and these also displayed slight variations yet maintained overall similarity in their values. The findings from these analyses are illustrated in Figure 14.

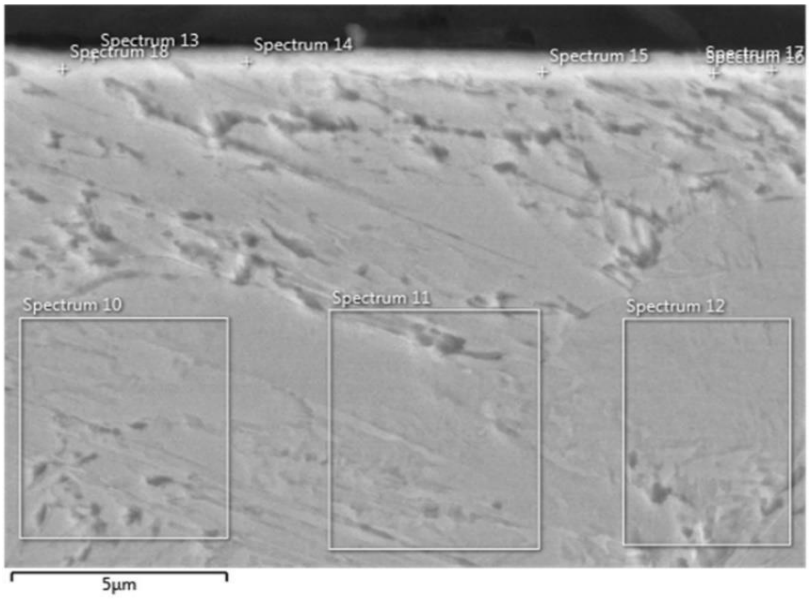

Figure 12: Location of the EDS spectra (10-18) conducted on sample C

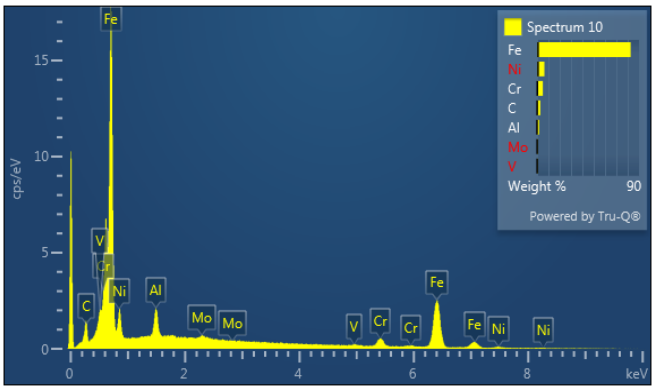

Spectrum 10	*Wt%*	*Wt% Sigma*
C	2.87	0.13
Al	1.87	0.06
V	0.46	0.14
Cr	5.13	0.22
Fe	82.55	0.89
Ni	6.50	0.94
Mo	0.63	0.16
Total	100.00	

Figure 13: EDS results of spectrum 10 on the bulk material of sample C

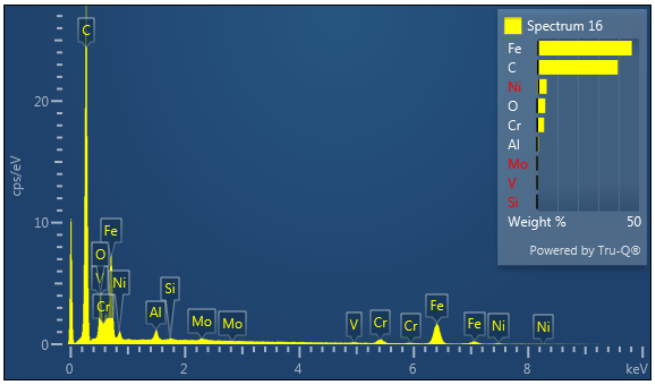

Spectrum 16	*Wt%*	*Wt% Sigma*
C	39.56	0.42
Al	0.71	0.03
V	0.46	0.10
Cr	3.49	0.16
Fe	46.41	0.50
Ni	4.70	0.68
Mo	0.55	0.10
Total	100.00	

Figure 14: EDS results of spectrum 16 on the surface layer of sample C

The comparison between Spectrum 10 from the bulk material and Spectrum 16 from the bright layer reveals some differences in their elemental compositions.

Carbon (C): There is a substantial increase in the carbon content in the bright layer (39.56%) compared to the bulk material (2.87%). However, this elevated carbon content in the bright

layer is attributed to the epoxy mounting material used during sample preparation, not the actual carbide content.

Aluminum (Al): The aluminum content is higher in the bulk material (1.87%) than in the bright layer (0.71%). This difference might indicate the depletion or migration of aluminum during the surface machining process.

Chromium (Cr): The chromium content is slightly lower in the bright layer (3.49%) compared to the bulk (5.13%). This slight reduction might suggest some chromium depletion in the surface layer during machining.

Iron (Fe): The iron content is considerably lower in the bright layer (46.41%) compared to the bulk material (82.55%). The lower iron content in the bright layer (Spectrum 16) is notable, as iron is the primary constituent of the Hybrid 60 alloy. This reduction is partly due to the high carbon signal from the epoxy, which skews the relative proportions of other elements detected in the analysis.

Nickel (Ni): The nickel content is slightly lower in the bright layer (4.70%) compared to the bulk material (6.50%). This minor difference might indicate nickel migration or depletion during the formation of the surface layer.

The EDS analysis demonstrates that the bright layer on the machined surface has a slightly different elemental composition compared to the bulk material. Additional EDS analysis was performed on the randomly distributed particles observed in the bulk material as shown in Figure 15. The results of this analysis are illustrated in Figures 16 and 17. These particles, which appear inconsistently throughout the bulk, were analyzed to understand their elemental composition and potential impact on the material's properties.

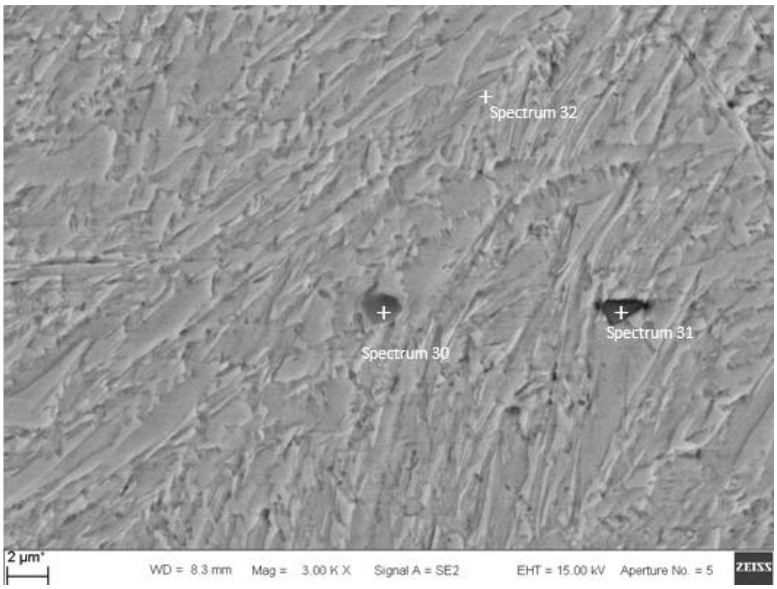

Figure 15: EDS spectrums conducted on particles in sample A

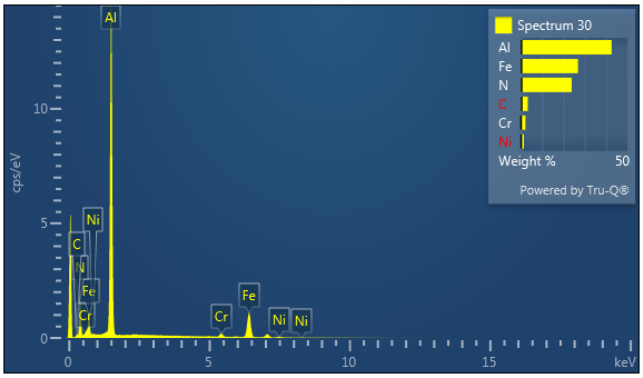

Spectrum 30	*Wt%*	*Wt% Sigma*
C	3.22	0.32
N	23.84	0.33
Al	42.63	0.29
Cr	2.14	0.11
Fe	26.79	0.28
Ni	1.38	0.17
Total	100.00	

Figure 16: EDS results of spectrum 30 on the bulk material of sample A

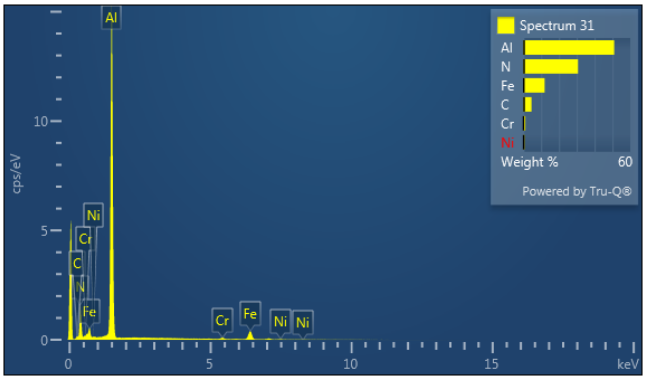

Spectrum 31	*Wt%*	*Wt% Sigma*
C	4.58	0.41
N	30.67	0.38
Al	50.99	0.38
Cr	1.12	0.10
Fe	11.96	0.24
Ni	0.67	0.16
Total	100.00	

Figure 17: EDS results of spectrum 31 on the bulk material of sample A

The EDS analysis results for the particles observed in the bulk material are presented in Spectrum 30 and Spectrum 31. The detailed compositions, illustrated in Figures 16 and 17, indicate that the particles are likely aluminum nitride (AlN) compounds, characterized by their high aluminum and nitrogen content. These compounds are randomly distributed and not consistent throughout the bulk material, suggesting they formed under specific conditions during the manufacturing process.

V-5- Hardness

Hybrid 60 has a known hardness of 60 HRC. The Vickers hardness values obtained from the measurements can be converted to compare with the HRC scale. Typically, for high-hardness materials, the conversion can be done using standard conversion charts.

The approximate conversion from Vickers hardness (HV) to Rockwell hardness (HRC) for high-hardness materials is:

$$HRC \approx 0.014 \times HV - 17.7$$

Using this formula, we can convert the Vickers hardness values obtained from the test:

Table 4: Hardness measurements results in both Vickers and Rockwell hardness

ROW ID	Hardness (HV)	Converted Hardness (HRC)
ROW 1	679 HV	60.2 HRC
ROW 2	675 HV	60.0 HRC
ROW 3	688 HV	61.0 HRC
ROW 4	682 HV	60.8 HRC
ROW 5	692 HV	61.0 HRC

The Vickers hardness test results for the Hybrid 60 samples show that the material possesses a uniform hardness distribution, with values closely matching the known hardness of 60 HRC. These measurements confirm the expected hardness properties of the Hybrid 60 material, ensuring its suitability for applications requiring high hardness.

V-6- Tool Wear

In this experiment, fresh cutting inserts were used to machine different samples using the hard turning technique. Stereo-microscopy images were taken for each of the inserts, as shown in Figure 18, to observe the differences in tool wear among the samples.

The insert used for Sample A, which was machined with a high cutting speed and a low feed rate for 123 meters, shows minimal wear with some slight edge degradation. This indicates that the combination of high cutting speed and low feed rate resulted in relatively moderate wear on the cutting insert during the hard turning process.

The insert for Sample B, machined with a low cutting speed and a low feed rate for 123 meters, exhibits slightly more wear compared to Sample A. The edge shows some rounding and minor chipping. The lower cutting speed results in less heat generation, possibly leading to more brittleness and gradual wear. The cutting insert for Sample C, machined with a high cutting speed and a high feed rate of 31 meters, displays minimal wear similar to Sample A.

The high cutting speed produces heat, reducing brittleness and minimizing tool wear despite the higher feed rate. For Sample D, machined for 31 meters with a low cutting speed and a high feed rate, the insert shows severe flank wear with prominent chipping and edge breakage. The low cutting speed combined with a high feed rate likely caused increased mechanical stress and brittleness, leading to substantial tool damage. The insert used for Sample E1, machined with medium cutting speed and feed rate for 49 meters, displays very minimal wear. The balanced cutting speed and feed rate produced a minimal level of tool wear, maintaining tool integrity effectively. The cutting insert for Sample E2, machined under the same medium cutting speed and feed rate as E1 for 49 meters, shows significant wear with visible chipping and edge degradation. This suggests that the cutting conditions for E2 were more aggressive or that there were variations in the material properties or machining conditions, resulting in higher wear compared to E1. Similar to E1, the insert for Sample E3, machined with medium cutting speed and feed rate for 49 meters, exhibits very minimal wear. The tool shows minor edge rounding and slight flank wear, indicating that the cutting conditions were well-balanced, leading to minimal tool damage.

The stereo-microscopy images clearly demonstrate the varying degrees of tool wear among the samples, influenced by the different cutting parameters used in hard turning. High cutting speeds (as seen in Samples A and C) tend to generate significant heat, reducing material brittleness and resulting in minimal tool wear despite the differences in feed rates. Samples machined with low cutting speeds and high feed rates (as seen in Sample D) show severe wear due to increased mechanical stress and brittleness. Moderate cutting conditions (as seen in Samples E1, E2, and E3) result in balanced wear, maintaining tool integrity for a longer duration.

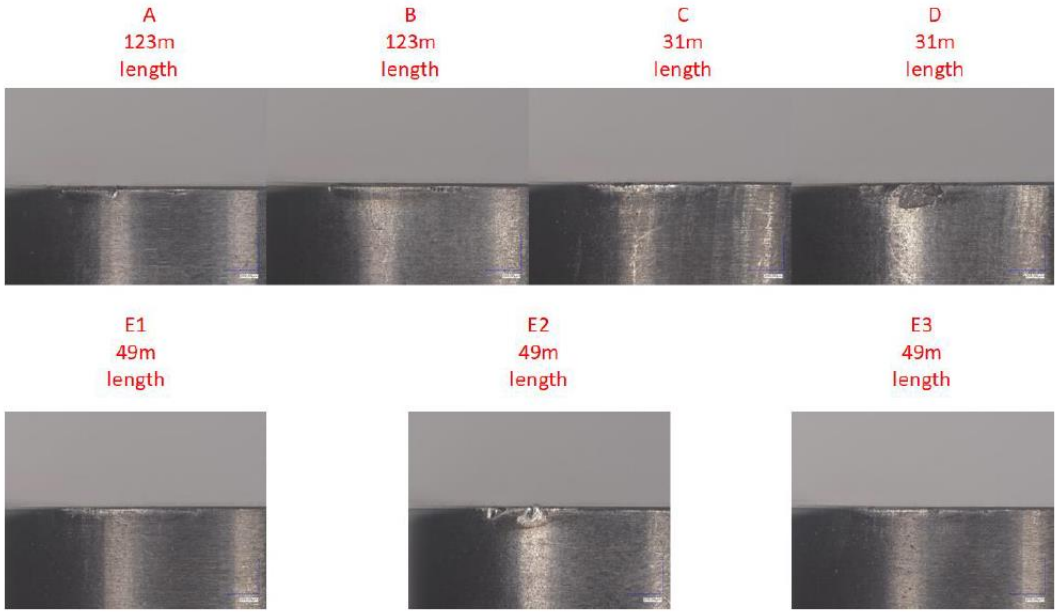

Figure 18: Images of the cutting inserts used for tool wear tests on the different samples

Chapter 6

VI- Discussion

VI-1- Residual stresses

The residual stress profiles in the cutting direction, as presented in the results section, revealed that all samples exhibit a characteristic hook-shaped pattern. This pattern indicates that the highest compressive stresses are found in the subsurface rather than at the surface, which aligns with the observations for hoop stresses.

In this experiment, the parameters varied were the feed rate and cutting speed. For the samples machined with a low feed rate, one was subjected to the highest cutting speed, while the other was machined at a lower speed. The sample machined with high cutting speed and low feed rate (sample A) have very low compressive stresses, as seen in the hoop stress plot in figure 4(a), while the sample machined with low cutting speed displayed relatively higher compressive stresses of about -100 MPa (Figure 4(a)). The low compressive stresses in the high-speed sample are attributed to the thermal stresses generated by the heat from the high cutting speed, whereas the compressive stresses in the low-speed sample result from mechanical stresses.

For the samples machined with high feed rate of 0.2 mm/rev, one was machined with high cutting speed of 200 m/min and the other with low cutting speed of 100 m/min, the sample machined with the lower cutting speed exhibited higher compressive residual stresses at the surface as shown in Figure 4, compared to the sample machined at the higher cutting speed. This difference is attributed to the thermal effects at high cutting speeds. As the cutting speed increases, the temperature also rises, which reduces the material's brittleness and results in lower compressive stresses.

At a subsurface depth of 5 µm, the compressive stresses increased, particularly in the sample machined with a high feed rate of 0.2 mm/rev and a low cutting speed of 100 m/min (Figure 5). This aligns with the characteristic hook-shaped residual stress profile, where subsurface compressive stresses are higher. The increase in subsurface compressive stresses is likely due

to the high cutting forces generated at the high feed rate, significantly increasing plastic deformation beneath the surface [26].

Samples E1, E2, and E3, machined with a medium feed rate of 0.125 mm/rev and a medium cutting speed of 150 m/min, followed the same general trends observed in the other samples, displaying compressive stresses at the surface that transitioned to tensile stresses at greater depths. The residual stress values for these samples were moderate compared to the other samples.

This behavior can be attributed to the balanced thermal and mechanical effects induced by the medium cutting parameters. At a medium cutting speed of 150 m/min, the temperature generated during machining is higher than that at low cutting speeds but lower than that at high cutting speeds. This moderate temperature rise helps to reduce material brittleness and thermal stresses, resulting in less severe compressive stresses compared to those at lower cutting speeds. However, the temperature is not high enough to cause significant thermal softening, which would further reduce the compressive stresses as seen in samples machined at higher cutting speeds. The medium feed rate of 0.125 mm/rev ensures that the cutting forces are balanced, avoiding the high mechanical stresses associated with high feed rates and the low mechanical stresses of low feed rates. This balance leads to moderate plastic deformation beneath the surface, contributing to the observed residual stress profiles.

VI-2- Surface roughness

Based on the surface roughness results, we can observe the impact of different cutting parameters on the average roughness (Ra) values as well as the other roughness parameters. The data shows that the highest values of Ra (1.065 µm and 1.026 µm) are generated with high feed rates (f = 0.2 mm/rev). In contrast, the lowest values of Ra (0.145 µm and 0.123 µm) are observed with low feed rates (f = 0.05 mm/rev). Samples machined with a medium feed rate (f = 0.125 mm/rev) produced intermediate Ra values (0.485 µm). This trend aligns with the general observations made by Grzesik [27], on C45 carbon steel, where the roughness average is a function of the feed rate. Additionally, for samples machined with the same feed rate but different cutting speeds, a slight change was observed. As the cutting speed increased from v_c = 100 m/min to v_c = 200 m/min, the roughness for samples machined with a low feed rate (f = 0.05 mm/rev) decreased. This reduction is attributed to the increase in surface temperature, which promotes the material softening phenomenon, leading to lower surface roughness which corelate with the observation made by Philip et al. [28] on hard turned AISI 52100 bearing steel.

However, for samples machined with a high feed rate, the sample machined at a higher cutting speed (v_c = 200 m/min) had a higher Ra compared to the sample machined at a lower cutting speed (v_c = 100 m/min). Interestingly, the values for Rz (4.256 µm) and Sa (1.118 µm) for the sample machined at the higher cutting speed were lower than those for the sample machined at the lower cutting speed (Rz = 4.270 µm and Sa = 1.206 µm). This difference in Ra could be due to inconsistency in surface roughness along the tested distance and tool wear (crater wear).

VI-3- Microstructure analysis

To investigate the metallurgical behavior of H60 when hard-turned with different feed rates and cutting speeds, SEM analysis was performed on the prepared samples, revealing various microstructural behaviors.

For sample A, machined with a cutting speed of 200 m/min and a feed rate of 0.05 mm/rev (Figure 9), a very thin layer (<1 µm) with a distinctly different microstructure from the bulk material was observed, indicating severe plastic deformation (SPD). Such deformation typically results from high cutting forces and elevated temperatures during machining [29]. Literature suggests that low cutting speeds generate significant mechanical stresses, leading to increased plastic deformation [29]. In samples machined with a low feed rate (0.05 mm/rev) and low cutting speed (100 m/min), as well as those with a high feed rate (0.2 mm/rev) at both low and high cutting speeds, and medium feed rate (0.125 mm/rev) at a medium cutting speed (150 m/min), a very thin bright layer (<1 µm) appeared on the machined surface. This phenomenon is similar to the thin white layer observed in laser-assisted milling (LAMill) machined nickel-based superalloy, specifically Inconel 718, where no significant grain deformation was noted, only a thin white layer (0.5 µm thick). EDS results indicated no diffusion of alloying elements or any significant difference in the chemical composition within this layer compared to the bulk.

The bright layer observed in H60 differs from the typical white layers seen on machined hardened steels, which generally exhibit a more refined and significantly thicker microstructure than what is visible in the SEM images of H60. To gain a deeper understanding of the microstructure, techniques such as TEM are recommended.

Chapter 7

VII- Conclusions

This study investigated the influence of cutting parameters on the surface integrity of hard-turned Hybrid 60 samples. The analysis revealed that all samples exhibited a characteristic hook-shaped residual stress profile, with the highest compressive stresses occurring subsurface. Samples machined at high feed rates (0.2 mm/rev) and low cutting speeds (100 m/min) showed the highest compressive stresses due to significant mechanical stresses, while high cutting speeds (200 m/min) introduced more thermal stresses. Surface roughness results indicated that higher feed rates led to higher Ra values, while lower feed rates and high cutting speeds resulted in smoother surfaces due to thermal softening. SEM analysis identified a very thin bright layer indicative of severe plastic deformation under various machining conditions, similar to observations in laser-assisted milling of nickel-based superalloys. The study concludes that feed rate and cutting speed significantly affect both the residual stress profiles and surface roughness, highlighting the need to optimize these parameters for improved surface integrity in hard turning processes.

References

[1] J.-E. Andersson and S. Ooi, Hybrid Steel® – The Next Step in Steel Evolution, Ovako R&D, 2019.

[2] H. B. Nayak and K. B. Rathod, A new method of hard turning of hardened workpieces: A review, *Materials Today: Proceedings*, vol. 82, pp. 356-362, 2023.

[3] M. A. Rhoads, E. L. Raymond, and W. M. Garrison Jr, High strength, high fatigue structural steel, US Patent 5,393,488, Feb. 1995.

[4] M. A. El Hakim, M. A. Shalaby, S. C. Veldhuis, and G. K. Dosbaeva, Effect of secondary hardening on cutting forces, cutting temperature, and tool wear in hard turning of high alloy tool steels, *Measurement*, vol. 65, pp. 233-238, Apr. 2015.

[5] J.-E. Andersson, F. Lindberg, and S. Ooi, "Hybrid steel and its potential for bearing applications," in Bearing Steel Technologies: 12th Volume, Progress in Bearing Steel Metallurgical Testing and Quality Assurance, ASTM International, 2020.

[6] J.Y.C. Fang, W.H. Liu, T. Yang, Y. Wu, and Z.B. Jiao, Multicomponent Precipitation and Strengthening in Intermetallic-Strengthened Alloys, *Front. Mater.*, vol. 9, article 931098, 28 June 2022.

[7] W.F. Gale and T.C. Totemeier, Smithells Metals Reference Book (Eighth Edition), 2004, pp. 38-1-38-38.

[8] J.-E. Andersson, F. Lindberg, and P. Ölund, Hybrid Steel Enhances Component Performance at Reduced Weight, Ovako Group Research and Development, 2023.

[9] M. Hofinger, M. Ognianov, C. Turk, H. Leitner, and R. Schnitzer, "Early stages of precipitate formation in a dual hardening steel," HTM Journal of Heat Treatment and Materials, vol. 74, no. 5, pp. 293–301, 2019.

[10] H. B. Nayak and K. B. Rathod, A new method of hard turning of hardened workpieces: A review, *Materials Today: Proceedings*, vol. 82, pp. 356-362, 2023.

[11] W Grzesik. Advanced Machining Processes of Metallic Materials – Theory, Modeling and Application Oxford Elsevier, 2008.

[12] Tönshoff HK, Arendt C, Amor RB. Cutting of Hardened Steel. Ann. CIRP 2000;49(2):547.

[13] Z. Hessainia, A. Belbah, M. A. Yallese, T. Mabrouki, and J.-F. Rigal, On the prediction of surface roughness in hard turning based on cutting parameters and tool vibrations, *Measurement*, vol. 46, no. 5, pp. 1671-1681, June 2013.

[14] E. Isakov, *Cutting Data for Turning of Steel*, Industrial Press Inc., 2007.

[15] Sumitomo Electric Hardmetal. (n.d.). *IT105 CBN Grade*. Retrieved June 17, 2024, from https://www.sumitomotool.com/en/products/product-details/it105-cbn-grade

[16] Hosseini, S. B. (2015). *White layer formation during hard turning of through hardened martensitic and bainitic AISI 52100 steel*. PhD thesis, Chalmers University of Technology.

[17] Sales, W. F., Schoop, J., da Silva, L. R. R., Machado, Á. R., & Jawahir, I. S. (2020). A review of surface integrity in machining of hardened steels. *Journal of Manufacturing Processes*, 58, 136-162.

[18] Hadi Sutanto and Jan Madl 2018 IOP Conf. Ser.: Mater. Sci. Eng. 420 012031.

[19] Uribe, T. L. (Year). *Microstructural decay in high-strength bearing steels under rolling contact fatigue*. Doctoral thesis, KTH Royal Institute of Technology.

[20] Bhushan, B. (Year). *Surface roughness analysis and measurement techniques*. The Ohio State University.

[21] Jouini, N., Revel, P., Thoquenne, G. (2020). Influence of surface integrity on fatigue life of bearing rings finished by precision hard turning and grinding. *Journal of Manufacturing Processes*, 57, 444-451.

[22] N. Jouini, P. Revel, P.E. Mazeran, M. Bigerelle The ability of precision hard turning to increase rolling contact fatigue life Tribol Int, 59 (2013), pp. 141-146

[23] H. A. Calderon, M. E. Fine and J. R. Weertman, “Coarsening and morphology of β′ particles in Fe-Ni-Al-Mo ferritic alloys,” Metallurgical Transactions A, vol. 19, p. 1135–1146, 1988.

[24] Javaheri, V., Sadeghpour, S., Karjalainen, P., Lindroos, M., Haiko, O., Sarmadi, N., Pallaspuro, S., Valtonen, K., Pahlevani, F., Laukkanen, A., Kömi, J. (2022). Formation of nanostructured surface layer, the white layer, through solid particles impingement during slurry erosion in a martensitic medium-carbon steel. *Wear*, 496–497, 204301.

[25] Olortegui-Yume, J., & Kwon, P. (2007). Tool wear mechanisms in machining. *International Journal of Machining and Machinability of Materials*, DOI: 10.1504/IJMMM.2007.015469.

[26] Patrik Dahlman, Fredrik Gunnberg, Michael Jacobson. The influence of rake angle, cutting feed and cutting depth on residual stresses in hardturning. Journal of Materials Processing Technology 2004;147:181-184.

[27] W Grzesik. A revised model for predicting surface roughness in turning. Wear 1996: 194:143-148.

[28] Philippe Revel, Nabil Jouini, Guillaume Thoquenne, Fabien Lefebvre. High precision hard turning of AISI 52100 bearing steel. Precision Engineering 2016;43:24-33.

[29] Segal, V. (2018). Review: Modes and Processes of Severe Plastic Deformation (SPD). *Engineered Performance Materials*, 2874 Laurel Ridge Ln, Howell, MI 48843, USA;

DEPARTMENT OF INDUSTIAL OF MATERIAL SCIENCE
CHALMERS UNIVERSITY OF TECHNOLOGY
Gothenburg, Sweden 2024
www.chalmers.se

CHALMERS
UNIVERSITY OF TECHNOLOGY